Supplement of Nat. Hazards Earth Syst. Sci., 22, 2359–2379, 2022
https://doi.org/10.5194/nhess-22-2359-2022-supplement

Natural Hazards and Earth System Sciences
Open Access
EGU

Supplement of

Storm surge hazard over Bengal delta: a probabilistic–deterministic modelling approach

Md Jamal Uddin Khan et al.

Correspondence to: Md Jamal Uddin Khan (jamal.khan@univ-lr.fr)

1 Bathymetry

The initial version of the bathymetry used in this study was first developed by Krien et al. (2016) combining the following datasets -

1. 4 (four) navigational charts from National Hydrographic Office (NHO), and 60 (sixty) charts from Inland Waterways Authority of India (IWAI) for Hooghly river. They amount to 16,500 and 123,000 digitized sounding points respectively.
2. 1 (one) chart from the Bangladesh Navy, and 3 (three) charts from the Mongla Port Authority.
3. River cross-sections from Bangladesh Water Development Board (BWDB).
4. A 50-m resolution digital topography model developed by the Center for Environmental Geographic Information Services (CEGIS) through dedicated surveying.

This dataset is supplemented by GEBCO (2009) and ETOPO2 (from 89.3E to 92.3E and from 19.90N to 21N approximately).

When compared with the global GEBCO dataset, GEBCO is found to be much shallower compared to this dataset, in average by about 3m. The comparison is discussed in detail in Krien et al. (2016).

The dataset developed by Krien et al. (2016) was further updated by Khan et al. (2019) by adding 34 new Navigational charts collected from the Bangladesh Navy. This amounts to 77,000 new digitized points shown in Figure S1.

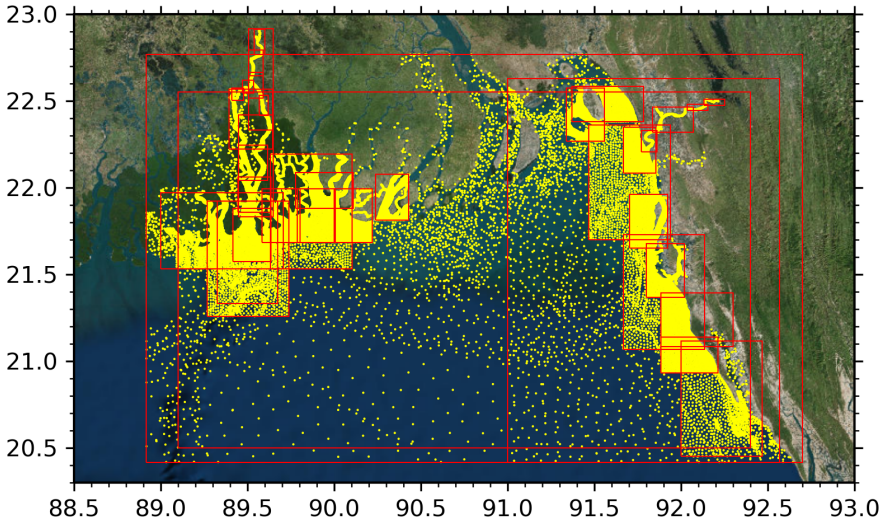

Figure S1. 77,000 digitized sounding points (in yellow). The coverage of the corresponding individual charts is shown in red outlines. The background image is taken from ESRI World Imagery services.

It is noteworthy here that, in Krien et al. (2016), embankments were also included as uniform height along the trace of the crests. For all embankments the same height was assumed (4.5m MSL). The embankment outlines were provided by the Bangladesh Water Development Board.

In the dataset assembled by Khan et al. (2019), that forms the basis of this paper, the crests heights still remain uniform over a single embankment, but replaced with respective measured (when available), or designed crest height for each embankment collected from BWDB. Figure of the crests heights are shown shown in Figure S2.

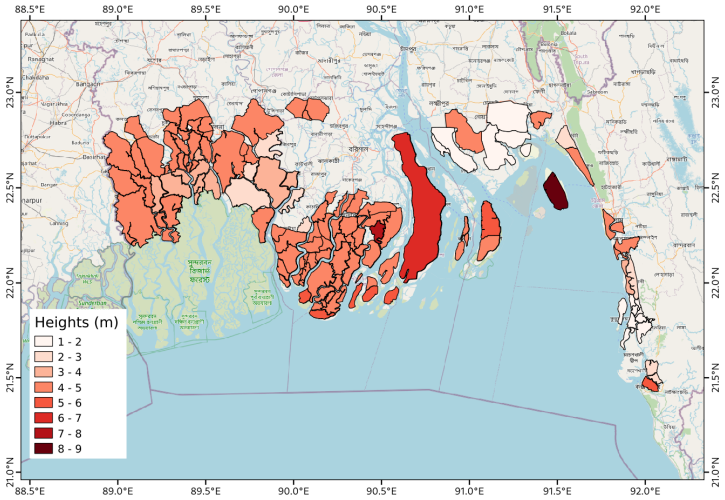

Figure S2. Embanked regions in the Bengal delta (polders) and their heights.

2 Tidal model validation

Our tidal model is validated at 7 tide gauge locations, around the Bengal delta. We have used complex error as the performance indicator (Mayet et al., 2013). The harmonic analysis is done using the Tidal toolbox developed at LEGOS (Allain, 2016). The modulus of the complex difference defines the complex error for a tidal constituent.

$$|\Delta z| = |A_m e^{i\phi_m} - A_o e^{i\phi_o}| \tag{S1}$$

Where A and ϕ are the amplitude and phase (in radians) respectively, of the tidal harmonics. The subscript denotes the model (m) and observation (o). The total error of all the constituent at one location is calculated as the squared root of half of the squared sum.

$$\sigma_s = \sqrt{\frac{1}{2}\sum_N |\Delta z|^2} \tag{S2}$$

Along the coast of Bengal delta, only four of the constituents - M2, S2, K1, and O1 are found to contribute significantly to the tidal energy (Sindhu and Unnikrishnan, 2013). As in many cases, information for other tidal harmonics is not available, only these four constituents are considered for calculating the total complex error at a location.

A comparison of the complex error between the global models and the model presented here is shown in Table S1. Amplitudes (A) and errors are in centimeter, phase (ϕ) is in degrees. Hooghly River, Diamond Harbour, Garden Reach and Chandpur are not represented in global tidal models (FES, GOT, and TPXO) due to their location in far upstream.

Table S1. Performance of tidal model at tide-gauge locations.

Station		Observation		FES2012-Hydro			FES2012			GOT4.8			TPXO7.2			This Model		
		A_0	ϕ_0	A_m	ϕ_m	Error	A_m	ϕ_m	Error	A_m	ϕ_m	Error	A_m	ϕ_m	Error	A_m	ϕ_m	Error
Sagar Roads (88.0300°E, 21.6500°N)	M2	140	116	142	99	42	137	104	29	113	113	27	132	104	28	144.5	114.9	5.3
	S2	66	150	73	141	13	62	141	11	40	145	40	48	126	29	62.4	153.3	5.2
	K1	15	262	17	256	2	16	253	3	14	277	14	14	258	1	15.6	265.4	1.1
	O1	5	250	6	251	1	6	243	1	5	270	2	5	252	0.4	5.7	251.6	0.8
	σ_s					**31**			**22**			**27**			**29**			**5.3**
Diamond Harbour (88.1733°E, 22.1928°N)	M2	157	168													142.3	165.6	15.9
	S2	68	210													57.6	208.6	10.4
	K1	15	285													13.2	286.3	1.8
	O1	7	258													5.4	257.7	1.6
	σ_s																	**13.6**
Hiron Point (89.4780°E, 21.8169°N)	M2	81	127	86	88	56	87	91	52	80	88	53	104	110	35	99.9	115.0	26.7
	S2	34	159	45	121	28	40	122	24	37	118	25	37	136	14	41.6	150.5	9.3
	K1	13	268	15	250	5	16	252	5	14	248	5	14	261	2	15.0	265.7	1.7
	O1	5	258	6	244	2	6	238	2	5	244	1	5	256	0.3	5.7	255.0	0.7
	σ_s					**44**			**40**			**42**			**27**			**20.0**
Dhulasar (90.2700°E, 21.8500°N)	M2	73	158	58	114	52	80	117	53	79	117	54	86	121	51	67.6	143.3	18.8
	S2	35	193	39	141	33	39	142	32	39	146	29	35	135	34	28.5	179.6	9.8
	K1	13	286	15	262	6	16	256	8	15	260	6	15	255	8	13.3	287.8	0.5
	O1	4	278	6	256	3	6	243	3	6	256	3	6	250	3	5.6	273.8	1.6
	σ_s					**44**			**44**			**44**			**44**			**15.0**
Charchanga (91.0500°E, 22.2188°N)	M2	96	234	110	202	57	115	208	50	97	204	49	84	154	103	95.8	216.9	28.5
	S2	37.5	265	38	238	18	30	243	15	34	234	19	36	186	47	36.6	250.3	9.5
	K1	13	304	17	298	4	16	300	4	7	314	6	16	272	8	16.8	308.7	4.0
	O1	8	285	7	289	1	6	284	2	4	303	4	6	267	3	8.1	293.1	1.1
	σ_s					**43**			**37**			**37**			**80**			**21.5**
Chittagong (91.8274 °E, 22.2434°N)	M2	173	196	118	193	56	126	200	49	120	192	54	89	153	123	149.2	194.8	24.1
	S2	64	229	41	230	23	33	236	31	43	227	21	40	160	62	55.0	225.8	9.6
	K1	19	278	17	294	6	17	295	6	9	300	11	16	258	7	19.1	284.9	2.3
	O1	8	263	7	285	3	6	280	3	4	289	5	6	252	2	7.9	267.3	0.6
	σ_s					**43**			**41**			**42**			**98**			**18.4**
Chandpur (90.6385°E, 23.2344°N)	M2	29.7	31.4													33.6	333.7	30.7
	S2	10.5	62.3													11.2	6.3	10.2
	K1	5.6	18.6													5.4	21.9	0.7
	O1	3.4	12.9													3.6	357.4	1
	σ_s																	**22.9**

3 Storm surge modelling

3.1 Underestimation in reanalysis wind fields

For the hindcast experiment for cyclone Sidr, shown in the manuscript - analytical wind fields are used. The general idea behind this experiment in the context of our manuscript is to show that analytical wind and pressure fields can correctly capture the recorded storm surges.

This choice of analytical fields raises a common question regarding the forcing strategy - namely what would have happened if the hindcasts were performed using available reanalysis wind and pressure field. The reanalysis fields are well known for underestimating severity of the cyclone - in both the cyclone maximum wind and the central pressure (Steptoe and Economou, 2021). To test it for cyclone Sidr, we compare the maximum wind speed and central pressure (minimum pressure resolved in the model grid) obtained from ERA5 and CFSR version 2 with the one obtained from JTWC Best track. The comparison is shown in Figure S3. From this comparison, it is clear reanalysis field vastly underestimate the maximum wind speed of the cyclone, as well as the drop in central pressure.

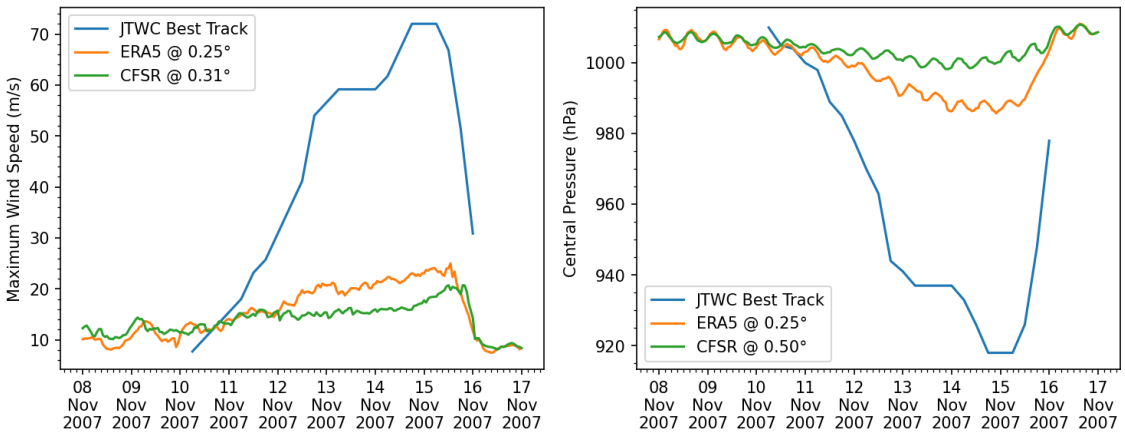

Figure S3. Comparison of Maximum wind speed (left) and Central pressure (right) among JTWC Best Track (blue), ERA5 (orange), and CFSR (green) during cyclone Sidr.

3.2 Wind and Pressure field formulas

We have used analytical formulas to derive the wind and pressure fields from the storm properties, i.e, location, maximum wind intensity (V_m), central pressure (P_c, and varies along the radial distance r. It is a very common practive in storm surge modelling to employ such analytical fields Lin and Chavas (2012).

For the pressure fields, we have used the Holland (1980) model. The pressure field along the radial distance r is described as following -

$$P(r) = P_c + \Delta P \exp\left(-\left(\frac{R_m}{r}\right)^B\right) \tag{S3}$$

with $B = \frac{V_m^2 e\rho + f V_m R_m e\rho}{\Delta P}$, $\rho = 1.15$, $e = \exp(1)$. ΔP is the pressure drop in the center from the ambient pressure (here taken as 1013 hPa).

Two radial wind profile formula has been used, viz., Emanuel and Rotunno (2011) and Holland (1980). The radial wind speed $V(r)$ in Emanuel and Rotunno (2011) is described by the following formula -

$$V(r) = \frac{2r(R_m V_m + 0.5 f R_m^2)}{R_m^2 + r^2} - \frac{fr}{2} \tag{S4}$$

where, R_m is the radius of maximum wind speed V_m.

The Holland (1980) wind field is described by the following formula -

$$V(r) = \sqrt{\left(\frac{R_m}{r}\right)^B \frac{B\Delta P \exp\left(-\left(\frac{R_m}{r}\right)^B\right)}{\rho} + \frac{r^2 f^2}{4}} - \frac{fr}{2} \tag{S5}$$

For both of the wind fields, an empirical surface wind reduction factor SWRF = 0.9, is used to convert the wind speed between 10m level and boundary layer level (Powell et al., 2003). According to the findings of Lin and Chavas (2012), the translation vector is reduced by a factor of $\alpha = 0.56$ and rotated counter-clockwise by an angle of $\beta = 19.2°$.

Analytical wind field formulas generally shows some bias compared to observations (Krien et al., 2018). To reduce such bias, we used a combination technique here based on the findings by Krien et al. (2018). By comparing the analytic fields with satellite scatterometer data, they showed that Emanuel and Rotunno (2011) model fits well to the inner core of the cyclone, and Holland (1980) fits well to the outer core. Hence, by combining these two analytical models the bias from a single analytical model is reduced.

We have used Emanuel and Rotunno (2011) model where $r < r_{50}$, and Holland (1980) model where $r > r_{50}$. r_{50} corresponds to the radius of 50-knots wind. For validation hindcast of Sidr, multiple raidal information were available from JTWC dataset, which is taken into account when solving for R_m in S5.

4 Comparsion of JTWC and cyclone ensemble

Figure 4 in the manuscript shows the comparison of the distribution of maximum wind speed and seasonal occurance between JTWC and cyclone ensemble. The errorbar in the JTWC values are computed based on the assumption that the number of events occurring in a month is a Poisson process. The location parameter in Poisson distribution (λ, here the number of events) for each month is computed by multiplying the probability density and number of JTWC events. Then from 10000 values generated from this distribution, the standard deviation is computed - which is the standard error reported in Figure 4 of the manuscript.

A second approach is also tested, using a bootstrap method, where a large set of samples (10000) of the same size as the JTWC dataset (42) is pulled from our ensemble. Then the monthly distribution is computed for the 10000 set, and the standard error is computed as the standard deviation of the 10000 instances for each month. Both the assumption of Poisson distribution and bootstrap method gives essentially similar results (Figure S4)

5 Extreme water level evolution in the Hooghly estuary

In Figure 8 of the manuscript we have noted a strong increase in extreme water level at higher return periods inside the Hooghly estuary. One possible reason is the amplification of higher levels of surges. In our 2020 paper (Khan et al., 2020), we show that tidal properties change substantially along the Hooghly estuary. To investigate we analyse two points from Figure 8 - Sagar Roads (located at 25km) and Diamond Harbour (located at about 100km).

First, we analyse the total water level at various return periods for these two locations (Figure S5). Two modelling configurations are used - one with full coupling of tide-surge-waves (solid line) and another is only tide-surge but without waves (dashed line). From the result, the contribution of waves in total water level is clear. The contribution varies among the two stations, but in general the amplification along the estuary remains the same as what we have reported in our manuscript - e.g., total water level amplifies after 100km compared to 50-year return period water level. This in turn indicates that the wave setup is not the component causing this amplification. Then the component that remains is the tide.

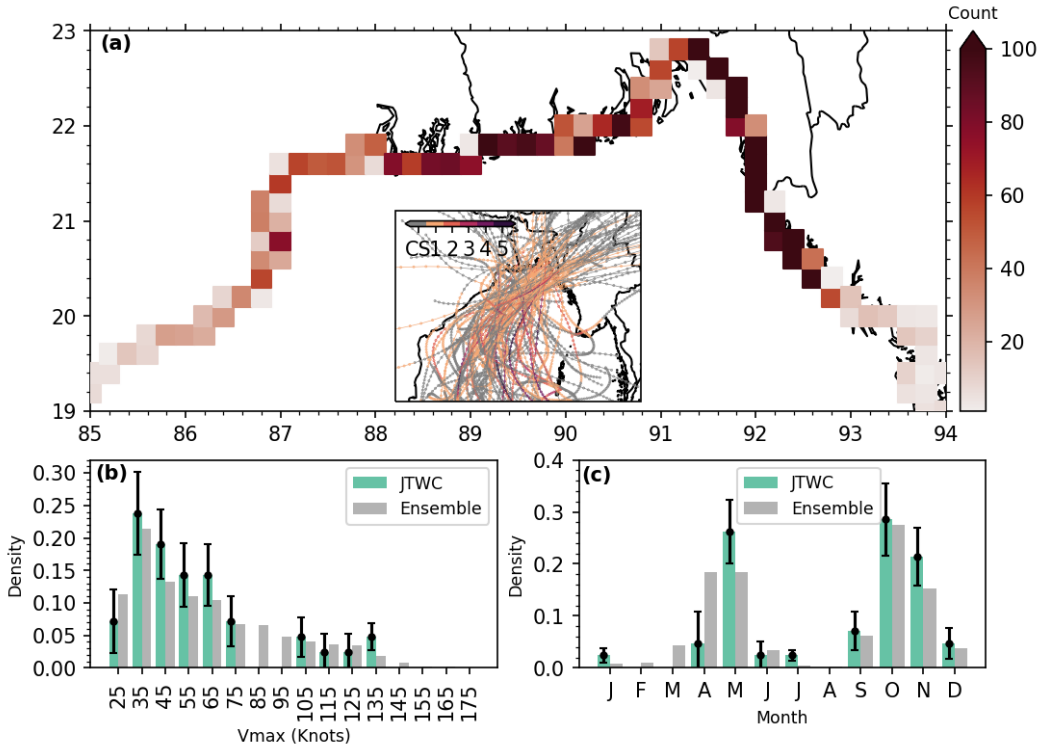

Figure S4. Same as Figure 4 in the manuscript, but the errorbar is computed using a bootstrap method.

Second, to see if the tide is creating the upstream amplification, we extracted the surge estimate from the tide-free version of the storm simulations ensemble. The mean water level is fixed at 0m MSL for these simulations. The surge at various return periods is shown in Figure S5, as a multiplication of the 50-year surge level. We see that between upstream and downstream the evolution of surge with a return period remains practically the same. This indicates the evolution of the total water level shown in Figure 8 is caused by the non-linear combination of tide, surge and wave-setup.

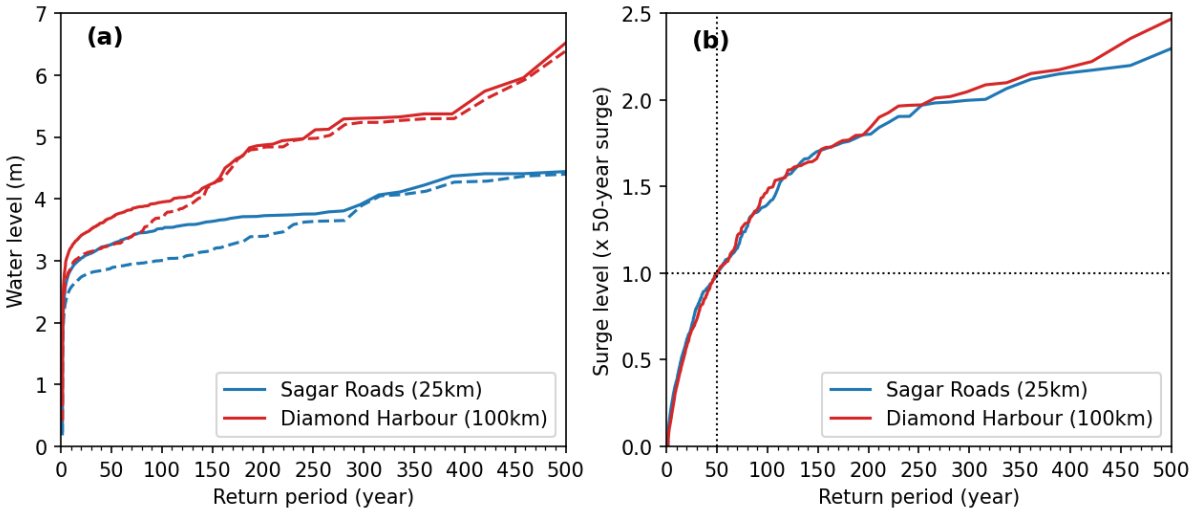

Figure S5. (a) Total water level at the given return periods for Sagar Roads (blue) and Diamond Harbour (red). The solid lines are from the ensemble simulation with coupled tide, surge and wave and the dashed lines are only coupled tide and surge but without waves. (b) Only surge level as multiple of 50-year surge level for Sagar Roads (blue) and Diamond Harbour (red). The surge level is simulated through the coupled wave model but without forcing any tide, i.e., always at mean sea level (MSL).

References

Allain, D. J.: TUGOm tidal toolbox, ftp://ftp.legos.obs, 2016.

Emanuel, K. and Rotunno, R.: Self-Stratification of Tropical Cyclone Outflow. Part I: Implications for Storm Structure, Journal of the Atmospheric Sciences, 68, 2236–2249, https://doi.org/10.1175/jas-d-10-05024.1, 2011.

Holland, G. J.: An Analytic Model of the Wind and Pressure Profiles in Hurricanes, Monthly Weather Review, 108, 1212–1218, https://doi.org/10.1175/1520-0493(1980)108<1212:aamotw>2.0.co;2, 1980.

Khan, M. J. U., Ansary, M. N., Durand, F., Testut, L., Ishaque, M., Calmant, S., Krien, Y., Islam, A. S., and Papa, F.: High-Resolution Intertidal Topography from Sentinel-2 Multi-Spectral Imagery: Synergy between Remote Sensing and Numerical Modeling, Remote Sensing, 11, 2888, https://doi.org/10.3390/rs11242888, 2019.

Khan, M. J. U., Durand, F., Testut, L., Krien, Y., and Islam, A. S.: Sea level rise inducing tidal modulation along the coasts of Bengal delta, Continental Shelf Research, 211, 104 289, https://doi.org/10.1016/j.csr.2020.104289, 2020.

Krien, Y., Mayet, C., Testut, L., Durand, F., Tazkia, A. R., Islam, A. K. M. S., Gopalakrishna, V. V., Becker, M., Calmant, S., Shum, C. K., Khan, Z. H., Papa, F., and Ballu, V.: Improved Bathymetric Dataset and Tidal Model for the Northern Bay of Bengal, Marine Geodesy, 39, 422–438, https://doi.org/10.1080/01490419.2016.1227405, 2016.

Krien, Y., Arnaud, G., Cécé, R., Ruf, C., Belmadani, A., Khan, J., Bernard, D., Islam, A., Durand, F., Testut, L., Palany, P., and Zahibo, N.: Can We Improve Parametric Cyclonic Wind Fields Using Recent Satellite Remote Sensing Data?, Remote Sensing, 10, 1963, https://doi.org/10.3390/rs10121963, 2018.

Lin, N. and Chavas, D.: On hurricane parametric wind and applications in storm surge modeling, Journal of Geophysical Research: Atmospheres, 117, n/a–n/a, https://doi.org/10.1029/2011jd017126, 2012.

Mayet, C., Testut, L., Legresy, B., Lescarmontier, L., and Lyard, F.: High-resolution barotropic modeling and the calving of the Mertz Glacier, East Antarctica, Journal of Geophysical Research: Oceans, 118, 5267–5279, https://doi.org/10.1002/jgrc.20339, 2013.

Powell, M. D., Vickery, P. J., and Reinhold, T. A.: Reduced drag coefficient for high wind speeds in tropical cyclones, Nature, 422, 279–283, https://doi.org/10.1038/nature01481, 2003.

Sindhu, B. and Unnikrishnan, A. S.: Characteristics of Tides in the Bay of Bengal, Marine Geodesy, 36, 377–407, https://doi.org/10.1080/01490419.2013.781088, 2013.

Steptoe, H. and Economou, T.: Extreme wind return periods from tropical cyclones in Bangladesh: insights from a high-resolution convection-permitting numerical model, Natural Hazards and Earth System Sciences, 21, 1313–1322, https://doi.org/10.5194/nhess-21-1313-2021, 2021.